

Almeida, T. P., Lequeux, S., Palomino, A., Sousa, R. C., Fruchart, O., Prejbeanu, I.-L., Dieny, B., Masseboeuf, A. and Cooper, D. (2022) Quantitative visualization of thermally enhanced perpendicular shape anisotropy STT-MRAM nanopillars. *Nano Letters*, 22(10), pp. 4000-4005. (doi: [10.1021/acs.nanolett.2c00597](https://doi.org/10.1021/acs.nanolett.2c00597))

There may be differences between this version and the published version. You are advised to consult the published version if you wish to cite from it.

<http://eprints.gla.ac.uk/271296/>

Deposited on 20 May 2022

Enlighten – Research publications by members of the University of Glasgow
<http://eprints.gla.ac.uk>

Quantitative visualization of thermally-enhanced perpendicular shape anisotropy STT-MRAM nano-pillars

Trevor P. Almeida^{1,2*}, Steven Lequeux³, Alvaro Palomino³, Ricardo C. Sousa³, Olivier Fruchart³, Ioan-Lucian Prejbeanu³, Bernard Dieny³, Aurélien Masseboeuf³ and David Cooper¹

¹Univ. Grenoble Alpes, CEA, Leti, F-38000 Grenoble, France.

²SUPA, School of Physics and Astronomy, University of Glasgow, G12 8QQ, UK.

³Univ. Grenoble Alpes, CEA, CNRS, Grenoble INP, SPINTEC, 38000 Grenoble, France.

Abstract

Perpendicular shape anisotropy (PSA) offers a practical solution to downscale spin-transfer torque Magnetoresistive Random-Access Memory (STT-MRAM) beyond the sub-20 nm technology node whilst retaining thermal stability. However, our understanding of the thermomagnetic behavior of PSA-STT-MRAM is often indirect, relying on magnetoresistance measurements and micromagnetic modelling. Here, the magnetism of a NiFe PSA-STT-MRAM nano-pillar is investigated using off-axis electron holography, providing spatially resolved magnetic information as a function of temperature. Magnetic induction maps reveal the micromagnetic configuration of the NiFe storage layer (~ 60 nm high, ≤ 20 nm diameter), confirming the PSA induced by its 3:1 aspect ratio. *In-situ* heating demonstrates that the PSA of the storage layer is maintained up to at least 250 °C, and direct quantitative measurements reveal a moderate decrease of magnetic induction. Hence, this study shows explicitly that PSA provides significant stability in STT-MRAM applications that require reliable performance over a range of operating temperatures.

Keywords: Perpendicular shape anisotropy STT MRAM; nanomagnetism; off-axis electron holography; thermomagnetic stability

*Corresponding author:

Tel: +44 (0) 141 330 4712

Email: trevor.almeida@glasgow.ac.uk

Magnetoresistive random-access memory (MRAM) is a type of non-volatile memory based on the storage of bits of information by magnetic cells with controllable polarity¹. The discovery of the spin-transfer torque (STT) effect has made MRAM industrially relevant, thanks to the ability to write cells with an electric current²⁻⁵. STT-MRAM can be easily integrated with CMOS technology⁶, has low energy consumption⁷, superior endurance^{7,8}, and rather high areal density⁹. In practice, STT-MRAM involves the use of a magnetic tunnel junction (MTJ) comprising two perpendicularly-magnetized ferromagnetic plates (one magnetically-pinned reference layer and one switchable storage layer) separated by a thin insulating MgO tunnel barrier (1 – 1.5 nm thick). This design is called p-STT-MRAM, the perpendicular anisotropy resulting from interfacial electronic hybridization effects occurring at the interface between the magnetic electrodes and the oxide tunnel barrier¹⁰. MTJs provide a useful system of readable / writable ‘0’ or ‘1’ binary information, as its electrical resistance changes significantly when the layers are magnetized in parallel and antiparallel states. Increasing the areal bit density of p-STT-MRAM requires to reduce the in-plane size or diameter of the nano-patterned MTJ¹¹. However, below a characteristic magnetic length scale around 20nm, this comes with an excessive decrease of the thermal stability of the magnetic moment of the ultrathin storage layer. Perpendicular shape anisotropy (PSA) offers an innovative solution by increasing the storage layer thickness to larger than its diameter, so that its out-of-plane aspect ratio combined with large volume provides additional thermal stability^{12,13}. PSA-STT-MRAM has been shown previously to indeed be highly thermally stable, making them a practical solution to downsize scalability of STT-MRAM at sub-20 nm technology nodes^{14,15}. However, our knowledge of the thermal stability of these STT-MRAM nano-pillars is often indirect, relying on magnetoresistance measurements and micromagnetic modelling. In order to understand fully their thermomagnetic behavior, it is necessary to examine the effect of temperature directly. The advanced transmission electron microscopy (TEM) technique of off-axis electron holography allows imaging of magnetization within nano-scale materials, with high spatial resolution and sensitivity to induction field components transverse to the electron beam¹⁶. Combining electron holography with *in-situ* heating within the TEM has already allowed direct imaging of the thermal stability of nano-scale signal carriers and fields of magnetic minerals¹⁷⁻¹⁹, meteorites²⁰ and pre-patterned MTJ conducting pillars²¹.

In this paper, we use electron holography to image the micromagnetic configuration of an individual ≤ 20 nm diameter FeCoB / NiFe STT-MRAM nano-pillar and acquire quantitative measurements of magnetic induction from the high-aspect-ratio FeCoB / NiFe composite free layer. In addition, we experimentally demonstrate the influence of PSA on its thermal stability

1 through *in-situ* heating within the TEM to 250 °C. This study provides direct evidence of the
2 PSA exhibited by the high-aspect-ratio free layer, and its improved thermal stability compared
3 to standard p-STT-MRAM.

4
5 An array of FeCoB / NiFe PSA-STT-MRAM nano-pillars was fabricated through sequential e-
6 beam lithography, reactive ion etching and ion beam etching¹². The full stack of PSA MTJs has
7 the following composition: SiO₂ / Pt (25 nm) / SAF / Ta (0.3 nm) / FeCoB (1.1 nm) / MgO (1.2
8 nm) / FeCoB (1.4 nm) / W (0.2 nm) / NiFe (60 nm) / Ta (1 nm) / Ru (3 nm) / Ta (150 nm), where
9 the thick NiFe layer provides the PSA^{12,14}. SAF stands for a synthetic antiferromagnet,
10 providing a compensated-moment antiferromagnetically-pinned magnetic reference as the
11 bottom layer. A protective layer of organic resin (~ 1 μm) was spin-coated onto the array prior
12 to being inserted into a Thermo Fisher Strata 400S dual-beam focused ion beam (FIB) /
13 secondary electron microscope (SEM) for TEM sample preparation. A protective W layer was
14 deposited over the resin and trenches were FIB irradiated until a ~ 3 μm × ~ 20 μm lamella was
15 prepared and transferred to Omniprobe copper lift-out grids, where it was thinned to a thickness
16 of ~ 300 nm using conventional FIB methods. The protective resist layer was etched away using
17 a plasma cleaner and the remaining W layer was broken off with the micromanipulator. High
18 angle annular dark field (HAADF) scanning TEM (STEM) imaging was performed using a
19 probe-C_s-corrected Thermo Fisher Titan TEM with an accelerating voltage of 200kV.
20 Corresponding chemical analysis was provided by energy dispersive X-ray (EDX)
21 spectroscopy using a Super-X EDX system whose geometry consists of four Bruker silicon drift
22 detectors. A Thermo Fisher Titan TEM equipped with an image-C_s corrector and an electron
23 biprism was used to perform off-axis electron holography. Electron holograms were acquired
24 under field-free conditions in Lorentz mode on a Gatan OneView 4K camera. A voltage of 220
25 V was applied to the biprism, resulting in an interference fringe spacing of ~ 1.7 nm. Stacks of
26 8 electron holograms (each acquired for 4s) were aligned and then averaged using the Holoview
27 software²² to improve the signal to noise ratio of the reconstructed phase images. The
28 magnetization states of the nano-pillars were visualized through separation of the magnetic
29 contribution to the phase shift from the mean inner potential (MIP), achieved by tilting to ± 40°
30 and applying the strong field of the objective lens (< 1.5 T) to reverse the magnetic
31 contribution²³. *In-situ* heating up to 250°C was performed using a Gatan heating holder under
32 field-free magnetic conditions, allowing 30 minutes to stabilize from thermal drift at each
33 temperature interval. The heating was repeated and the magnetic reversal was performed at
34 each temperature interval to isolate the MIP, and subtracted from the first heating to reconstruct

1 the thermomagnetic behavior of the nano-pillars^{18,19}. For the construction of magnetic induction
2 maps, the cosine of the magnetic contribution to the phase shift was amplified ($\times 150$) to
3 produce magnetic phase contours and arrows were added to show the direction of the projected
4 induction.

5
6 Figure 1 presents the chemical composition, morphology and structure of an individual nano-
7 pillar from the etched FeCoB / NiFe stack. The HAADF STEM image (Fig. 1a) displays the
8 general morphology of the nano-pillar with a distinct difference in Z-contrast between the top
9 Ta mask and lower shaft. This is confirmed by EDX chemical mapping of Fig. 1b, revealing
10 the dimensions of the NiFe section of the nano-pillar (~ 60 nm high, diameter of ≤ 20 nm), and
11 that the ~ 3 nm Ru layer separates it from the hard Ta mask. The O signal is dispersed across
12 the entire nano-pillar and its physical state is explored through precession diffraction acquired
13 from the boxed region (red) in the EDX chemical map of Fig. 1c. The precession data presented
14 in Figs 1d & 1e is created by summing all the scanned diffraction patterns in the boxed region
15 of Fig 1c into one diffraction pattern. Integrated signals are then extracted separately from the
16 diffuse diffraction ring and crystalline diffraction spots to provide an overview of their
17 respective contributions. The weakly crystalline / amorphous state of the surface of the nano-
18 pillar highlighted in the scanned area of Fig. 1d (left) is demonstrated in the associated electron
19 diffraction image (right). Conversely, Fig. 1e shows the crystalline state of the center of the
20 nano-pillar in the scanned area (left) and associated electron diffraction (right). The line profile
21 of Fig. 1f is acquired from the red arrow in Fig. 1c (averaged vertically over ~ 15 nm) and
22 displays the cross-section of normalized x-rays % for Fe, Ni and O content. The Ni and Fe
23 profiles overlap consistently and the diffraction data of Fig. 1e demonstrates a homogeneous,
24 crystalline NiFe core of the nano-pillar with measured composition of 81 at% Ni and 19 at%
25 Fe. The O-rich phase is confined to the surface and considering its weakly crystalline /
26 amorphous state, is largely attributed to residual organic resin from the preparation process.

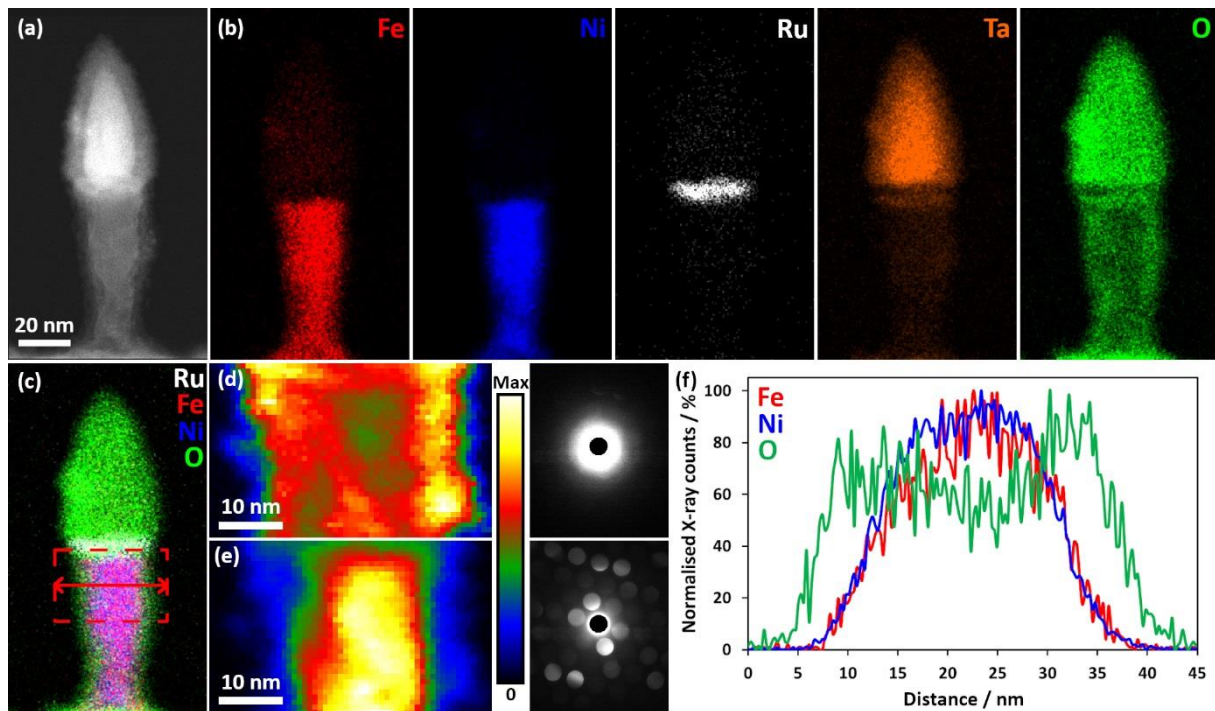


Figure 1. Overview of the morphology, chemical composition and structural properties of the nano-pillar. (a) HAADF STEM image of the nano-pillar; and (b) associated EDX chemical maps showing the elemental distribution of iron, nickel, ruthenium, tantalum and oxygen. (c) EDX chemical map highlighting the iron / nickel-rich center and oxygen-rich surface of the nano-pillar. (d,e) Precession electron diffraction acquired from the boxed region (red) in (c), showing the (d) amorphous surface; and (e) crystalline core. The colored scale bar denotes the normalized electron intensity between zero and maximum intensity. (f) Elemental line profile acquired along the red arrow in (c) and averaged vertically over ~ 15 nm, displaying the cross-section of normalized x-rays % for iron, nickel and oxygen content.

Figure 2 presents phase information reconstructed from electron holography of the nano-pillar, including quantification of magnetic induction and associated magnetization. The electron hologram of Fig. 2a shows the morphology of the nano-pillar at the same magnification as the associated projected magnetic induction map (Fig. 2b), which clearly demonstrates the existence of a magnetic dipole within the nano-pillar. This is emphasized by superimposing the associated magnetic induction over the EDX chemical map (Fig. 2c), where the magnetic contours flow along the major axis of the NiFe section. A line profile of the magnetic phase contribution (ϕ_m) acquired along the white arrow in Fig. 2c (averaged vertically over ~ 15 nm) is overlaid over the chemical profile from the same region (Fig. 2d). The magnetic phase shift $\Delta\phi_m$ in the pillar can be used to quantify the integrated in-plane magnetic induction related to the nano-pillar, where the minimum and maximum ϕ_m values [Fig. 2c, dotted vertical lines (pink)] coincide with the full width half maximum of the Ni / Fe chemical profiles. Extracting quantitative calculations of magnetization from such local observations must be handled with care as it displays integrated information (see Supplementary materials for details on the calculations summarized below). At first approximation, the nano-pillar can be treated as a

uniformly-magnetized infinite cylinder of radius r . The magnetic induction transverse to the electron beam direction is considered to arise from magnetization only (neglecting dipolar fields, *i.e.*, stray field and internal demagnetizing field) and can be estimated with the Aharonov-Bohm effect using a radius of ~ 8.6 nm (obtained from Fig. 2d). A first value of $\mu_0 M_s = 0.82 \pm 0.06$ T is extracted with the standard deviation determined from the noise of free space. To better quantify this important parameter, we can estimate the associated demagnetizing field of such a structure with the F_{ijk} functions from Hubert's formalism using a prism approach²⁴, at the exact same location of the measurement of the integrated magnetic flux obtained with the phase slope. We then obtain a better estimation of $\mu_0 M_s = 1.19 \pm 0.08$ T with the removal of the integrated demagnetizing and stray field globally antiparallel to magnetization, which lowered our first approximation. Subsequently, to overcome the geometrical approximation for the integrated demagnetizing field estimation with a prismatic geometry, we performed a tomographic reconstruction through inverse Abel transformation²⁵ to extract the magnetic flux density in the core vicinity of the cylinder. The resulting value was finally adjusted with the local estimation of demagnetizing field through F_{ijk} functions, as the tomography method helps to deconvolve the B field but not the internal H_d . Our final extraction leads to a value for the spontaneous magnetization induction of the NiFe nano-pillar of **$\mu_0 M_s = 1.14 \pm 0.01$ T**. Considering the geometric approximation for the pillar is only estimated at one position of the structure, this value is substantially more precise and is in reasonable agreement with the spontaneous induction for a $\text{Ni}_{81}\text{Fe}_{19}$ chemical composition, expected to reach 1.05 T²⁶. We ascribe the difference to uncertainties related to the exact value of the composition of the alloy the diameter of the PSA, and the sharpness of its outer surface. Due the small size of the nano-pillar, the position along the nano-pillar axis of direct ϕ_m measurement can also have a marked effect on the magnitude of the stray field, as shown in larger Co and Fe nanowires²⁷. Being systematic, these errors are expected to have no impact on the thermomagnetic measurements reported in the following section. More details in our analysis of this quantification are given in the supplementary materials.

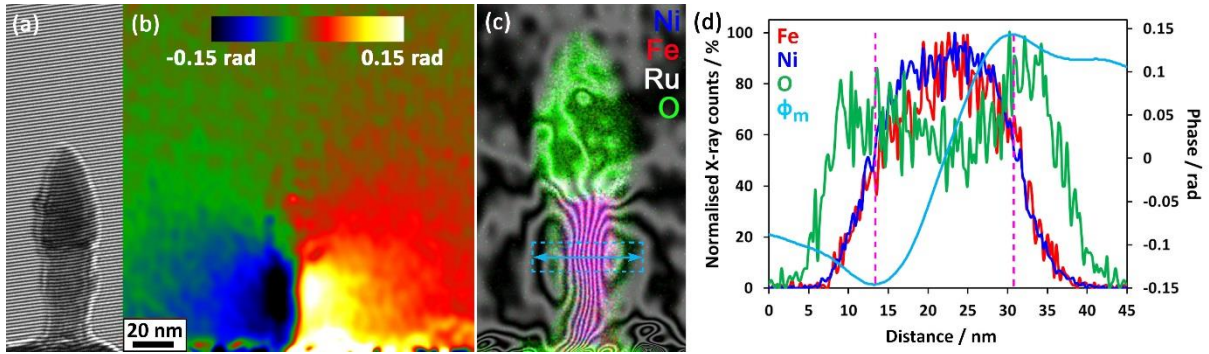


Figure 2. Overview of the magnetic induction associated with the nano-pillar and its quantification. (a) Electron hologram of the nano-pillar; and (b) reconstructed magnetic contribution to the total phase, revealing the PSA along its major axis. (c) Combined EDX / magnetic induction map showing magnetic contours flowing along the major axis of the NiFe section. The contour spacing is 0.042 rad (cosine amplified by 150 times). (d) Line profile acquired along the white arrow in (c) and averaged vertically over ~ 15 nm around the mid-height of the PSA free layer, superimposing the cross-section of magnetic phase over the chemical profile.

Figure 3 presents the thermomagnetic behavior of the nano-pillar during *in-situ* heating from room temperature to 250 °C. The initial combined EDX / magnetic induction map of Fig. 3a displays the nano-pillar at 20 °C, with the magnetization pointing from the bottom to the top of the NiFe free layer and confirming its PSA. The associated magnetic induction maps of Figs 3b-h display the same nano-pillar during heating from 100 °C to 250 °C at 25 °C intervals. It is evident that the NiFe section retains its upward direction of magnetization at all temperatures up to 250 °C. The thermomagnetic stability of the NiFe section in the nano-pillar is supported by Figure 4, which presents corresponding quantitative measurements of magnetic induction at each temperature interval. The $\Delta\phi_m$ was measured from the same area presented in Fig. 2c,d and \vec{B} calculated using equation S2 (Supplementary information), which is proportional to magnetization. The average value of $B \rightarrow$ is $\sim 0.8 \pm 0.06$ T and the trend-line exhibits a decrease of ~ 0.08 T between 20 °C and 250 °C, which is in good agreement with a ~ 0.09 T decrease over the same temperature range in bulk permalloy ($\text{Ni}_{80}\text{Fe}_{20}$)^{28,29}. If heated to higher temperatures, the nano-pillar would be expected to follow the same bulk properties and become paramagnetic at a Curie temperature around ~ 575 °C^{28,29}. As the contribution of the dipolar field to the measured induction field is proportional to magnetization for PSA, we expected that Fig.4 is representative of the thermal decay of magnetization in the PSA.

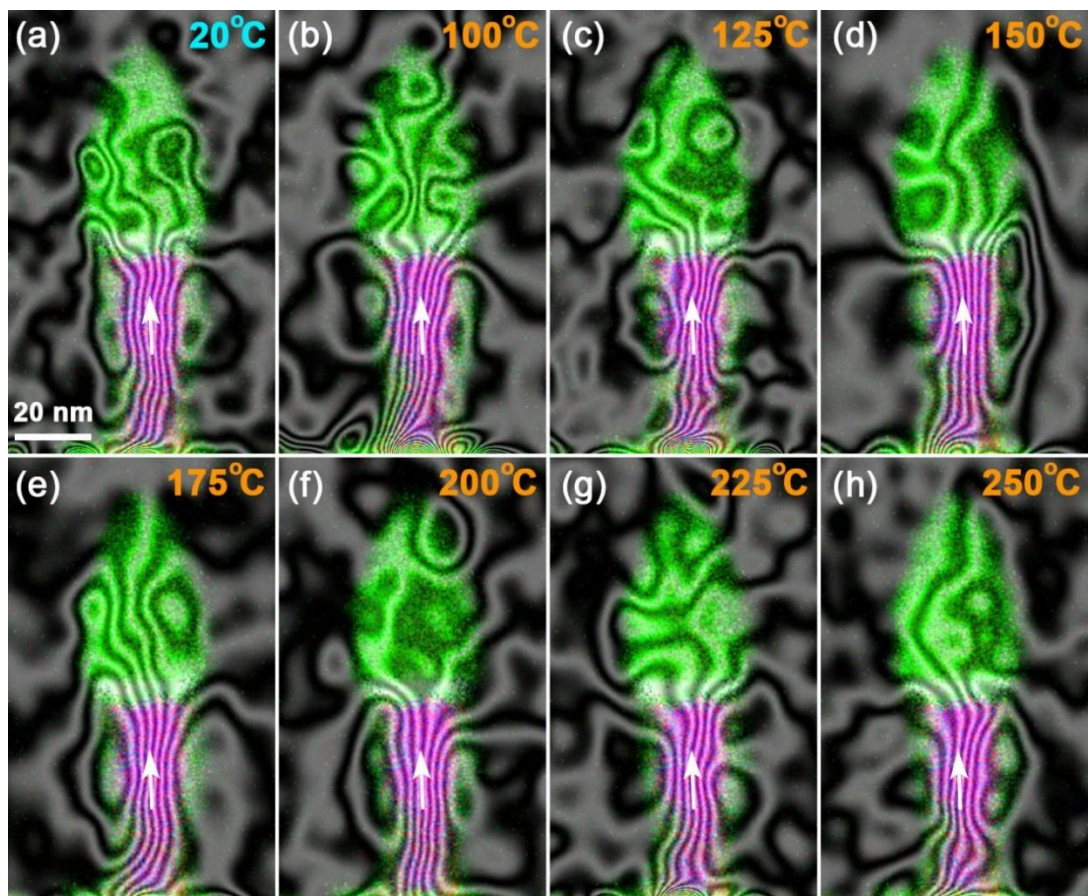


Figure 3. Visualization of the thermomagnetic stability within the nano-pillar. (a-h) Combined EDX / magnetic induction maps showing the PSA in the NiFe section of the nano-pillar acquired at (a) 20 °C; or during *in-situ* heating at 25 °C intervals from (b) 100 °C to (h) 250 °C. The contour spacing is 0.042 rad for all the magnetic induction maps (cosine multiplied by 150 times) and the magnetization direction is shown using arrows.

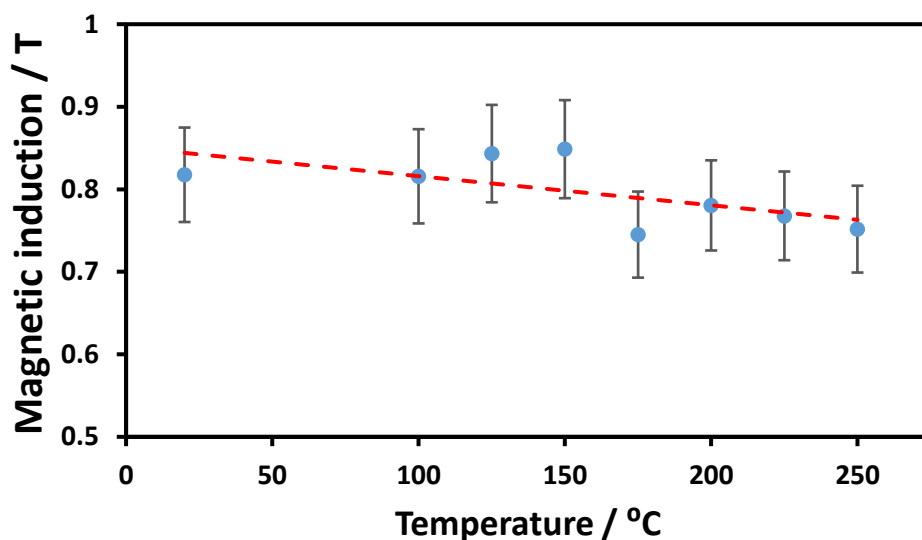


Figure 4. Magnetic induction associated to the nano-pillar as a function of temperature. Calculated magnetic induction transverse to the electron beam using the direct measurement of magnetic contribution to the phase from the NiFe section shown in Figure 3 with temperature, i.e., including a contribution from the demagnetizing and stray fields globally opposite to magnetization in the pillar, from 20 °C to 250 °C.

The main reason to fabricate STT-MRAM nano-pillars with PSA is to stabilize and preserve the magnetic configuration of the free FeCoB / NiFe composite layer in response to temperature fluctuations during operation. It is evident from the *in-situ* heating TEM experiment that the dipolar magnetic orientation along the major axis of the NiFe section (bottom to top) is retained at all temperature intervals up to at least 250 °C. In addition, the associated direct measurements of \vec{B} (average $\approx 0.8\text{T} \pm 0.06\text{T}$) did not vary sufficiently to suggest a change in magnetic orientation, nor magnetization. The slight decreasing trend in magnitude of \vec{B} is attributed to an expected reduction in spontaneous magnetization when heating towards the Curie temperature³⁰, as would be observed in the same bulk material. As the shape-anisotropy energy barrier of the nano-pillar scales linearly with M_S^2 , this confirms that the energy barrier of switching between parallel and anti-parallel states has not been exceeded up to at least 250 °C, and the PSA has provided significant thermal stability compared to standard p-STT-MRAM stacks based on ultrathin films¹²⁻¹⁵. In standard p-STT-MRAM, the spontaneous magnetization may indeed decrease by a few tens of percent at 250°C due to enhanced fluctuations in low-dimensions for the ultrathin films involved, and the energy barrier associated with perpendicular anisotropy may decrease even more as it relies on interfacial magnetic anisotropy, which suffers from enhanced thermal decay due to its two-dimensional nature³¹⁻³³. Further, the maximum temperature of *in-situ* heating used (250 °C) far exceeds the operating temperatures for a range of STT-MRAM device applications, including commercial (70 °C), industrial (85 °C), automotive (125 °C) and military (150 °C)³⁴. It is also comparable to the temperature of reflow soldering used to attach chips to a printed circuit board (260 °C)³⁵. This thermal stability is crucial for many FLASH-replacement applications in which the program code is loaded in the chip prior to reflow soldering.

In conclusion, this electron holography study has provided explicit evidence of the PSA in ≤ 20 nm diameter p-STT-MRAM nano-pillar; previously only measured indirectly by magnetoresistance measurements and micromagnetic modelling. The enhanced thermal stability of PSA-STT-MRAM, compared with standard p-STT MRAM based on these films, has been confirmed by both imaging and quantitative measurements from their magnetic configuration during *in-situ* heating. This supports the use of PSA-STT-MRAM in a variety of applications that require reliable performance over a range of operating temperatures.

Supporting Information: Quantitative analyses of the dipolar field and spontaneous magnetization of the nano-pillar.

References:

1. B. Dieny, *et al.*, Opportunities and challenges for spintronics in microelectronics industry, *Nat. Electron.* 2020, **3**, 446-459.
2. S. Bhatti, *et al.*, Spintronics based random access memory: a review, *Mater. Today.* 2017, **20**, 530-548.
3. S. Ikeda, *et al.*, A perpendicular-anisotropy CoFeB–MgO magnetic tunnel junction, *Nat. Mater.*, 2010, **9**, 721.
4. A. D. Kent, Spintronics: Perpendicular all the way, *Nat. Mater.*, 2010, **9**, 699.
5. T. Liu, Y. Zhang, J. W. Cai and H. Y. Pan, Thermally robust Mo/CoFeB/MgO trilayers with strong perpendicular magnetic anisotropy, *Sci. Rep.*, 2015, **4**, 5895.
6. D. McGrath, Intel says FinFET-based embedded MRAM is production-ready, *EE Times*, <https://www.eetimes.com/intel-says-finfet-based-embedded-mram-is-production-ready/>, (accessed 08/13/2021).
7. Apalkov, D., Dieny, B. & Slaughter, J. M. Magnetoresistive random access memory. *Proc. IEEE*, 2016, **104**, 1796–1830.
8. Khvalkovskiy, A. V. et al. Basic principles of STT-MRAM cell operation in memory arrays. *J. Phys. D.* 2013, **46**, 074001.
9. S.-W. Chung, T. Kishi, J.W. Park, M. Yoshikawa, K. S. Park, T. Nagase, K. Sunouchi, H. Kanaya, G.C. Kim, K. Noma, M. S. Lee, A. Yamamoto, K. M. Rho, K. Tsuchida, S. J. Chung, J. Y. Yi, H. S. Kim, Y.S. Chun, H. Oyamatsu and S. J. Hong, *Proceedings of the 2016 IEDM conference*, 2016, 27.1.
10. B. Dieny and M. Chshiev, Perpendicular magnetic anisotropy at transition metal/oxide interfaces and applications. *Rev. Mod. Phys.*, 2017, **89**, 025008.
11. V. D. Nguyen, P. Sabon, J. Chatterjee, L. Tille, P. Veloso Coelho, S. Auffret, R. Sousa, L. Prejbeanu, E. Gautier, L. Vila and B. Dieny, Novel approach for nano-patterning magnetic tunnel junctions stacks at narrow pitch: A route towards high density STT-MRAM applications, *2017 IEEE International Electron Devices Meeting (IEDM)*, 2017, DOI: 10.1109/IEDM.2017.8268517.
12. N. Perrissin, S. Lequeux, N. Strelkov, A. Chavent, L. Vila, L. D. Buda-Prejbeanu, S. Auffret, R. C. Sousa, I. L. Prejbeanu and B. Dieny, A highly thermally stable sub-20 nm magnetic random-access memory based on perpendicular shape anisotropy, *Nanoscale*, 2018, **10**, 12187.

13. K. Watanabe, B. Jinnai, S. Fukami, H. Sato and H. Ohno, Shape anisotropy revisited in single-digit nanometer magnetic tunnel junctions, *Nat. Commun.* 2018, **9**, 663.
14. N. Perrissin, N. Caçoilo, G. Gregoire, S. Lequeux, L. Tillie, N. Strelkov, A. Chavent, S. Auffret, L. D. Buda-Prejbeanu, R. C. Sousa, L. Vila, I. L. Prejbeanu and B. Dieny, Perpendicular shape anisotropy spin transfer torque magnetic random-access memory: towards sub-10 nm devices. *J. Phys. D: Appl. Phys.*, 2019, **52**, 505005.
15. S. Lequeux, N. Perrissin, G. Grégoire, L. Tillie, A. Chavent, N. Strelkov, L. Vila, L. D. Buda-Prejbeanu, S. Auffret, R. C. Sousa, I. L. Prejbeanu, E. Di Russo, E. Gautier, A. P. Conlan, D. Cooper and B. Dieny, Thermal robustness of magnetic tunnel junctions with perpendicular shape anisotropy, *Nanoscale*, 2020, **12**, 6378.
16. V. Boureau, M. Stano, J-L. Rouvière, J-C. Toussaint, O. Fruchart and D. Cooper, High-sensitivity mapping of magnetic induction fields with nanometer-scale resolution: comparison of off-axis electron holography and PDPC, *J. Phys. D: Appl. Phys.* 2021, **54**, 085001.
17. T. P. Almeida, T. Kasama, A. R. Muxworthy, W. Williams, and R. E. Dunin-Borkowski, Observing thermomagnetic stability of non-ideal magnetite particles: Good paleomagnetic recorders? *Geophys. Res. Lett.* 2014, **41**, 7041.
18. T. P. Almeida, A. R. Muxworthy, A. Kovács, W. Williams, P. D. Brown, and R. E. Dunin-Borkowski, Direct visualization of the thermomagnetic behavior of pseudo-single-domain magnetite particles, *Sci. Adv.* 2016, **2**, e1501801.
19. T. P. Almeida, A. R. Muxworthy, A. Kovács, W. Williams, L. Nagy, P. Ó Conbhuí, C. Frandsen, R. Supakulopas, and R. E. Dunin-Borkowski, Direct observation of the thermal demagnetization of a vortex structure held by a non-ideal magnetite recorder, *Geophys. Res. Lett.* 2016, **43**, 8426.
20. J. Shah, W. Williams, T. P. Almeida, L. Nagy, A. R. Muxworthy, A. Kovács, M. A. Valdez-Grijalva, K. Fabian, S. S. Russell, M. J. Genge and R. E. Dunin-Borkowski, The oldest magnetic record in our solar system identified using nanometric imaging and numerical modeling, *Nat. Commun.* 2018, **9**, 1173.
21. V. Boureau, V. D. Nguyen, A. Masseboeuf, A. Palomino, E. Gautier, J. Chatterjee, S. Lequeux, S. Auffret, L. Vila, R. Sousa, L. Prejbeanu, D. Cooper and B. Dieny, An electron holography study of perpendicular magnetic tunnel junctions nanostructured by deposition on pre-patterned conducting pillars, *Nanoscale*, 2020, **12**, 17312.

22. V. Boureau, R. McLeod, B. Mayall and D. Cooper, Off-axis electron holography combining summation of hologram series with double-exposure phase-shifting: Theory and application, *Ultramicroscopy*, 2018, **193**, 52-63.
23. T. P. Almeida, T. Kasama, A. R. Muxworthy, W. Williams, L. Nagy, T. W. Hansen, P. D. Brown and R. E. Dunin-Borkowski, Visualized effect of oxidation on magnetic recording fidelity in pseudo-single-domain magnetite particles, *Nat. Commun.* 2014, **5**, 5154.
24. A. Hubert and R. Schafer, *Magnetic Domains. The Analysis of Magnetic Microstructures*, Springer-Verlag, Berlin, Heidelberg, New York, 1998.
25. C. Phatak, L. de Knoop, F. Houdellier, C. Gatel, M. J. Hÿtch and A. Masseboeuf, Quantitative 3D electromagnetic field determination of 1D nanostructures from single projection, *Ultramicroscopy*, 2016, **164**, 24-30.
26. R. D. Tikhonov and A. A. Cheremisinov, Magnetization of Permalloy Films, *Russian Microelectronics*, 2017, **46 (2)**, 95–104.
27. K. Chai, Z. Li, W. Huang, G. Richter, R. Liu, B. Zou, J. Caron, A. Kovács, R. E. Dunin-Borkowski and J. Li, Magnetic quantification of single-crystalline Fe and Co nanowires via off-axis electron holography, *J. Chem. Phys.* 2020, 152, 114202.
28. A. B. Johnston, J. N. Chapman, B. Khamsehpour and C. D. W. Wilkinson, *In situ* studies of the properties of micrometre-sized magnetic elements by coherent Foucault imaging, *J. Phys. D: Appl. Phys.* 1996, **29**, 1419–1427.
29. R. M. Bozorth, 1964 *Ferromagnetism* (New York: Van Nostrand) p 112.
30. X. Zhang, Y. Lao, J. Sklenar, N. S. Bingham, J. T. Batley, J. D. Watts, C. Nisoli, C. Leighton and P. Schiffer, Understanding thermal annealing of artificial spin ice, *APL Mater.* 2019, **7**, 111112.
31. H. Sato, E. C. I. Enobio, M. Yamanouchi, S. Ikeda, S. Fukami, S. Kanai, F. Matsukura and H. Ohno, Properties of magnetic tunnel junctions with a MgO/CoFeB/Ta/CoFeB/MgO recording structure down to junction diameter of 11 nm *Appl. Phys. Lett.*, 2014, **105**, 062403.
32. H. Sato, S. Ikeda and H. Ohno, Magnetic tunnel junctions with perpendicular easy axis at junction diameter of less than 20 nm *Jpn. J. Appl. Phys.*, **2017**, 56, 0802A6.
33. L. Thomas, G. Jan, J. Zhu, H. Liu, Y.-J. Lee, S. Le, R.-Y. Tong, K. Pi, Y.-J. Wang, D. Shen, R. He, J. Haq, J. Teng, V. Lam, K. Huang, T. Zhong, T. Torng and P.-K. Wang, Perpendicular spin transfer torque magnetic random access memories with high spin

torque efficiency and thermal stability for embedded applications (invited), *J. Appl. Phys.*, 2014, **115**, 172615.

34. J. M. Iwata-Harms, G. Jan, H. Liu, S. Serrano-Guisan, J. Zhu, L. Thomas, R-Y. Tong, V. Sundar and P-K. Wang, High-temperature thermal stability driven by magnetization dilution in CoFeB free layers for spin-transfer torque magnetic random access memory, *Sci. Rep.* 2018, **8**, 14409.

35. Meng-Chun Shih et al., "Reliability study of perpendicular STT-MRAM as emerging embedded memory qualified for reflow soldering at 260°C," *2016 IEEE Symposium on VLSI Technology*, 2016, pp. 1-2, doi: 10.1109/VLSIT.2016.7573411.

Funding

This work, carried out on the Platform for Nanocharacterisation (PFNC), was supported by the “Recherches Technologiques de Base” program of the French National Research Agency (ANR) via Carnot Funding and the European Research Council (ERC MAGICAL, 669204).

Table of Content graphic

